

RESEARCH

Open Access



Intravitreal delivery of NMO-IgG causes primary retinal damage in the absence of optic nerve injury

Biyue Chen^{1,2,3†}, Huanfen Zhou^{1†}, Mingming Sun^{1†}, Wanqun Yang^{5,7†}, Qianqian Li^{5†}, Kaishu Yang⁵, Honglu Song^{1,4}, Quangang Xu¹, Xintong Xu^{1,2}, Yuyu Li¹, Yanyan Yu⁵, Shihui Wei^{1,2*} and Tingjun Chen^{5,6*}

Abstract

Background Neuromyelitis Optica (NMO) is a neuroimmune disorder primarily driven by autoantibodies against aquaporin 4 (AQP4), known as NMO-IgG. Although the mechanisms underlying NMO-IgG-induced retinopathy are not fully understood, the high expression of AQP4 in retinal Müller cells suggests a direct interaction that may trigger inflammatory processes in the retina. Previous studies indicate that microglia play a critical role in mediating immune responses, leading to neuronal dysfunction.

Methods NMO-IgG obtained from clinical patients was administered via intravitreal injection to female C57BL/6 mice. Techniques such as optical coherence tomography (OCT), Flash Visual Evoked Potential (f-VEP), electroretinography (ERG), real-time fluorescence quantitative PCR (RT-qPCR), and immunofluorescence analyses were used to assess retinal changes. The potential for reversing retinopathy was explored by depleting microglial cells using the CSF1 receptor inhibitor PLX3397. Additionally, a Transwell co-culture system of MIO-M1 (Müller cells) and BV2 (microglia) cells was established to study their interactions.

Results Intravitreal injection of purified NMO-IgG in mouse models led to its deposition in the retina and downregulation of AQP4 in provided. Vascular leakage was observed, alongside retinal dysfunction characterized by thinning of the retinal nerve fiber layer (RNFL) and loss of retinal ganglion cells (RGCs). On day 7, C3 expression was upregulated in Müller cells, followed by microglial activation. Significant morphological changes in microglia were noted, with increased expression of iNOS and C1q, indicating substantial activation. Ablating microglia significantly mitigated NMO-IgG-induced injury to RGCs. In vitro, NMO-IgG-treated MIO-M1 cells secreted higher levels of C3, enhancing the activation and migration of BV2 cells compared to controls.

Conclusions The retinal dysfunction observed in NMO may primarily be linked to the activation of Müller cells by NMO-IgG, leading to increased C3 secretion, which in turn activates microglia. Therapeutic strategies targeting Müller cell–microglia interactions in NMO-IgG-induced retinopathy could be promising in addressing the underlying retinal pathology in this condition.

Keywords NMO, Retinopathy, Müller cells, Microglia, C3, C1q

[†]Biyue Chen, Huanfen Zhou, Mingming Sun, Wanqun Yang, and Qianqian Li contributed equally to this work.

*Correspondence:

Shihui Wei

weishihui706@hotmail.com

Tingjun Chen

chentingj@uor.edu.cn; chentingj@uhrs.edu.cn

Full list of author information is available at the end of the article



Background

Neuromyelitis optica spectrum disorder (NMOSD) is an autoimmune inflammatory demyelinating condition that predominantly affects the optic nerve and spinal cord within the central nervous system (CNS) [1–3]. Patients with NMOSD-associated optic neuritis (ON) frequently exhibit thinning of the ganglion cell and inner plexiform layer (GCIPL) and the RNFL, indicating neuronal and axonal degeneration [4]. Interestingly, research suggests that subclinical visual function and structural abnormalities may be present even in the eyes without optic neuritis of NMOSD patients, which indicates that primary retinal injury might precede the onset of optic neuritis in NMO [5]. This primary retinal pathology could potentially lead to significant vision and visual field impairments independent of optic nerve damage.

More than 70% of NMO patients are seropositive for an autoantibody (NMO-IgG or AQP4-IgG) that targets the water channel protein aquaporin-4 (AQP4), a key pathogenic factor in NMOSD [6]. In early studies, the co-injection of NMO-IgG and human complement induced pathology resembling neuromyelitis optica (NMO) in animal brains [7], demonstrating that autoantibody-mediated complement-dependent cytotoxicity (CDC) is critical to NMO pathology. However, in primary astrocyte cultures, the binding of this autoantibody to aquaporin-4 (AQP4) can trigger AQP4 internalization, leading to an inflammatory response in astrocytes [8, 9]. This process may subsequently induce secondary demyelination and axonal loss.

Recently, new translational research has revealed that in over 50% of NMO patients, NMO-IgG primarily induces AQP4 internalization, which suppresses autoantibody-induced CDC by reducing the binding sites for complement components on astrocytes [10]. Moreover, clinical neuropathological observations have highlighted prominent microglial activation in the early stages of NMO, underscoring the significance of microglia in NMO pathogenesis [11]. Building upon this new understanding, we developed a novel animal model that uncovered unexpected interactions between astrocytes and microglia within spinal cord lesions characteristic of the NMO model [12, 13]. Over the past three years, research from our team and others has demonstrated that either NMO-IgG or AQP4 autoantibodies are sufficient to induce NMO pathology even in the absence of exogenous complement components [14, 15].

Müller cells—abundant in the retina—share many similarities with astrocytes and are sometimes categorized within the same cluster [16]. Whether AQP4 internalization induced by NMO-IgG also triggers interactions between Müller cells and microglia leading to microglia-mediated retinopathy remains an open question.

In this study, we developed a new mouse model of NMO-IgG-associated retinopathy. Our results demonstrate that NMO-IgG induces RGC injury, leading to abnormalities in electroretinography (ERG) and optical coherence tomography (OCT). Microglial activation is an early hallmark in this model, and depletion of microglia significantly rescues RGC damage induced by NMO-IgG. Furthermore, *in vitro* studies revealed that NMO-IgG stimulates Müller cells to produce complement C3, which activated microglia to release complement C1q, thereby inducing neuronal dysfunction. Our findings suggest that microglia may serve as a promising therapeutic target for primary retinopathy in NMOSD.

Materials and methods

Patient samples and human IgG purification

Blood samples were collected from four healthy controls (HCs) and four patients diagnosed with Neuromyelitis Optica Spectrum Disorder (NMOSD) at the Ophthalmology Department of the Chinese People's Liberation Army (PLA) General Hospital. The selected patients were seropositive for AQP4-IgG, as confirmed by a cell-based indirect immunofluorescence assay, and were diagnosed according to the 2015 International Consensus Diagnostic Criteria [17]. Exclusion criteria included the presence of other immune disorders, infections, or cancer. Patient demographics, including age, sex, and disease duration, are summarized in Table 1. The medication history of patients with NMO is summarized in Table 2. None of the healthy controls had a history of disease or infection, and none had received any treatment in the preceding two months. Informed consent was obtained from all participants.

Serum samples were heat-inactivated at 56 °C for 30 min to deactivate complement proteins. Total IgG was purified from 4 ml of pooled serum from NMOSD patients and healthy controls using a protein-A column (GE Healthcare Bio-sciences, USA) and concentrated with Amicon Ultra-4 centrifugal filters (50 kDa, Merck Millipore, Germany). The concentration of total IgG was 1.38 mg/ml based on the test result with the BCA method (Abbkine; # KTD3001). The purified IgG was diluted to 4 ml with phosphate-buffered saline (PBS) and sterilized using a 0.2 µm filter.

Animals and intravitreal injection

Female C57BL/6 mice aged 6–8 weeks and weighing 20–25 g were obtained from SPF Biotechnology (License No. SCKK 2019-0010, Beijing, China) and housed under controlled conditions with a 12-h dark/light cycle, with free access to food and water. All experimental protocols adhered to the Statement for the Use of Animals in

Table 1 Demographic and clinical characteristics of NMOSD patients and healthy controls

	Age (years)	Sex (M/F)	AQP4-IgG titer		MOG-IgG titer	Disease duration (months)
			CSF	Plasma	Plasma	
Patient 1	52	F	1:3.2	1:1000	–	11
Patient 2	31	F	1:1	1:1000	–	20
Patient 3	50	F	–	1:1000	–	3
Patient 4	45	F	1:3.2	1:1000	–	9
Control 1	42	M	–	–	–	–
Control 2	42	F	–	–	–	–
Control 3	31	F	–	–	–	–
Control 4	40	F	–	–	–	–

Ophthalmic and Vision Research and were approved by the Institutional Animal Care and Research Advisory Committee of the PLA General Hospital (Approval number: 2021-X17-08).

Mice were anesthetized via intraperitoneal injection of sodium pentobarbital. Intravitreal injections of 2 μ l purified NMO-IgG were administered to the right eyes of the mice, while the left eyes served as controls and received equal volumes of purified HC-IgG. To prevent leakage, the needle was kept in place for an additional minute post-injection. Retinal circulation was confirmed by assessing the color of the retinal vessels, and antibiotic ointment was applied to prevent infection.

Pharmacological ablation of microglia

To deplete retinal microglia, mice were fed a diet containing the colony-stimulating factor 1 receptor (CSF1R) inhibitor PLX3397 (600 mg/kg, Moldiets, China) starting 7 days before the intravitreal injection and continuing until sacrifice. Control groups were fed an AIN76A chow diet, which had the same composition as the experimental diet but lacked PLX3397. The effectiveness of microglial ablation was evaluated by immunostaining retinal tissue sections.

Evans blue assay

A 2% (w/v) solution of Evans Blue dye (Sigma-Aldrich, St. Louis, Missouri, USA) was injected via the tail vein, followed by a 2-h circulation period. After circulation, eyeballs were collected and immersed in 4% paraformaldehyde (PFA) for 2 h. The retinas were carefully dissected and shaped into a four-leaf clover configuration. Blood-retinal barrier (BRB) integrity was examined using a microscope (Olympus, Japan) with an excitation wavelength of 594 nm.

Immunofluorescence staining

After anesthesia, mice were perfused with saline and 4% PFA. Eyeballs were then fixed with 4% PFA for 1 h at room temperature (RT). For flat mounts, retinas were dissected and rinsed with PBS containing 0.1% Tween (PBST). For frozen sections, eyeballs were dehydrated in sucrose at increasing concentrations (10%, 20%, and 30%) after fixation. Following the removal of corneas and lenses, the eyeball cups were embedded in O.C.T. and frozen at -80°C . Cross-sections (12 μ m) were obtained using a Thermo cryostat (CRYOSTAR NX50, Thermo, USA) and mounted onto microscope slides.

Tissues were blocked with PBS containing 5% bovine serum albumin and 0.1% Triton X-100 (blocking buffer) and incubated with primary antibodies overnight at 4°C . After washing with PBST, tissues were incubated with secondary antibodies for 1 h at RT, followed by counterstaining with DAPI. Images were captured using the Operetta CLS High-Content Analysis System (PerkinElmer, Waltham, MA, USA) or a confocal imaging system (Olympus FV100, Olympus, Japan).

The antibodies used included mouse anti-AQP4 (ab9512, Abcam, 1:100), rabbit anti-AQP4 (A5971, Sigma, 1:500), mouse anti-GFAP (MAB360, Sigma, 1:500), rabbit anti-IBA-1 (ab178846, Abcam, 1:500), rat anti-IBA-1 (ab283346, Abcam, 1:100), rabbit anti-GS (PA5-28940, Thermo Scientific, 1:250), rat anti-C3 (ab11862, Abcam, 1:50), rabbit anti-RBPMS (PA5-31231, Invitrogen, 1:500), mouse anti-C1q (ab182452, Abcam, 1:10), rat anti-C1q (ab11861, Abcam, 1:50), mouse anti-iNOS (sc-7271, Santa Cruz, 1:100), rat anti-CD31 (ab56299, Abcam, 1:400), rabbit anti-MBP (ab40390, Abcam, 1:400), and goat anti-human IgG Alexa Fluor 488 (A11013, Invitrogen, 1:200). The concentrations of the second antibodies were 1:500.

Images were analyzed using Fiji software (National Institutes of Health, Bethesda, MD, USA). The average RGC count was calculated using two fields from each

Table 2 Medical history of NMO/D patients

	Number of episodes	Duration of disease at sample collection (weeks)	Medication history
Patient 1	2	4	Received no treatment this time. No previous use of immunosuppressor treatment
Patient 2	3	12	Received no treatment this time. No previous use of immunosuppressor treatment
Patient 3	2	1	Treated with oral corticosteroids 10 mg per day for 5 days. No previous use of immunosuppressor treatment
Patient 4	3	4	Treated with intravenous high dose corticosteroids followed by tapering. No previous use of immunosuppressor treatment

retinal quadrant in flat mounts. AQP4 signals were quantified by measuring immunofluorescence intensity at vascular walls, and signal intensity along lines was determined using the ImageJ plot profile. Colocalization was quantified using Pearson's correlation coefficient via the JACoP plugin in ImageJ [18].

Hematoxylin and eosin (H&E) staining

Mice were euthanized by cervical dislocation, and retinas were promptly isolated, fixed in 4% PFA, embedded in paraffin, and sectioned at a thickness of 4 μ m. The paraffin-embedded eye sections were stained with hematoxylin and eosin (H&E) for histological examination. Images were captured using a light microscope (Olympus, Japan).

RT-qPCR assessment

Total RNA was extracted from retinas and cultured cells using TRIzol reagent (Vazyme, Nanjing, China) following the manufacturer's protocol. Complementary DNA (cDNA) was synthesized using the PrimeScript RT Reagent Kit (RR047A, Takara, Tokyo, Japan) for reverse transcription of mRNA. Quantitative real-time PCR (RT-qPCR) was performed with UltraSYBR Mixture (CW0957M, CW Biotech Co., Beijing, China) on the CFX96 RT-PCR system (CFX96 Optics Module; Bio-Rad, USA).

The sequences of mouse primers used were as follows:

- GAPDH: Forward: 5'-AGGTCGGTGTGAACG GATTTG-3'; Reverse: 5'-TGTAGACCATGTAGT TGAGGTCA-3'.
- C3: Forward: 5'-CCAGCTCCCCATTAGCTC TG-3'; Reverse: 5'-GCACTTGCCCTCTTTAGGA AGTC-3'.
- C1q: Forward: 5'-AAAGGCAATCCAGGCAAT ATCA-3'; Reverse: 5'-TGGTTCTGGTATGGACTC TCC-3'.
- iNOS: Forward: 5'-GTTCTCAGCCCAACAATA CAAGA-3'; Reverse: 5'-GTGGACGGGTTCGATG TCAC-3'.
- Arg-1: Forward: 5'-CCTGAAGGAACTGAAAGG AAAG-3'; Reverse: 5'-TTGGCAGATATGCAG GGAGT-3'.

The sequences of human primers used were as follows:

- GAPDH: Forward: 5'-GGAGCGAGATCCCTCCAA AAT-3'; Reverse: 5'-GGCTGTTGTCATACTTCT CATGG-3'.
- AQP4: Forward: 5'-TCAGCATCGCCAAGTCTG TC-3'; Reverse: 5'-CTGGGAGGTGTGACCAGA TAG-3'.
- C3: Forward: 5'-GGCTGTCTTCTCTCAAGCA-3'; Reverse: 5'-GGGAATCTCACACATCACTCT-3'.

(See figure on next page.)

Fig. 1 Intravitreal injection of NMO-IgG induced AQP4 loss in retina. **a** Schematic timeline of the experimental design. **b** Immunofluorescence of AQP4 and human IgG in retinal flat mounts 3 days (D3) post-intravitreal injection of 2 μ l purified HC-IgG or NMO-IgG in mice (Scale bar = 50 μ m). **c** Confocal immunofluorescence images of retinal sections stained for AQP4 (red) and GS (green) with merged images (Scale bar = 20 μ m). **d** Quantification of the relative fluorescence intensity corresponding to (c) (n = 4 per group). **e** Left: Immunofluorescence of AQP4 (green) and CD31 (red) in retinal flat mounts highlighting vascular structures positive for CD31. Middle: Enlarged views of the dashed box areas, which were used for plot profile measurements. Right: Signal channel views of AQP4 and CD31. **f** Line intensity profiles from (e) indicating reduced perivascular AQP4 expression. **g** Fluorescent staining of Tunnel in retinas treated with HC-IgG or NMO-IgG on day 7 after Intravitreal injection. **h, i** AQP4 (red) and MBP (green) in the proximal optic nerve at 21 days post-modeling. MBP visualizes myelin sheaths with no significant demyelination or AQP4 loss observed in the optic nerve (Scale bar = 20 μ m). ** p < 0.01, *** p < 0.001, t-test

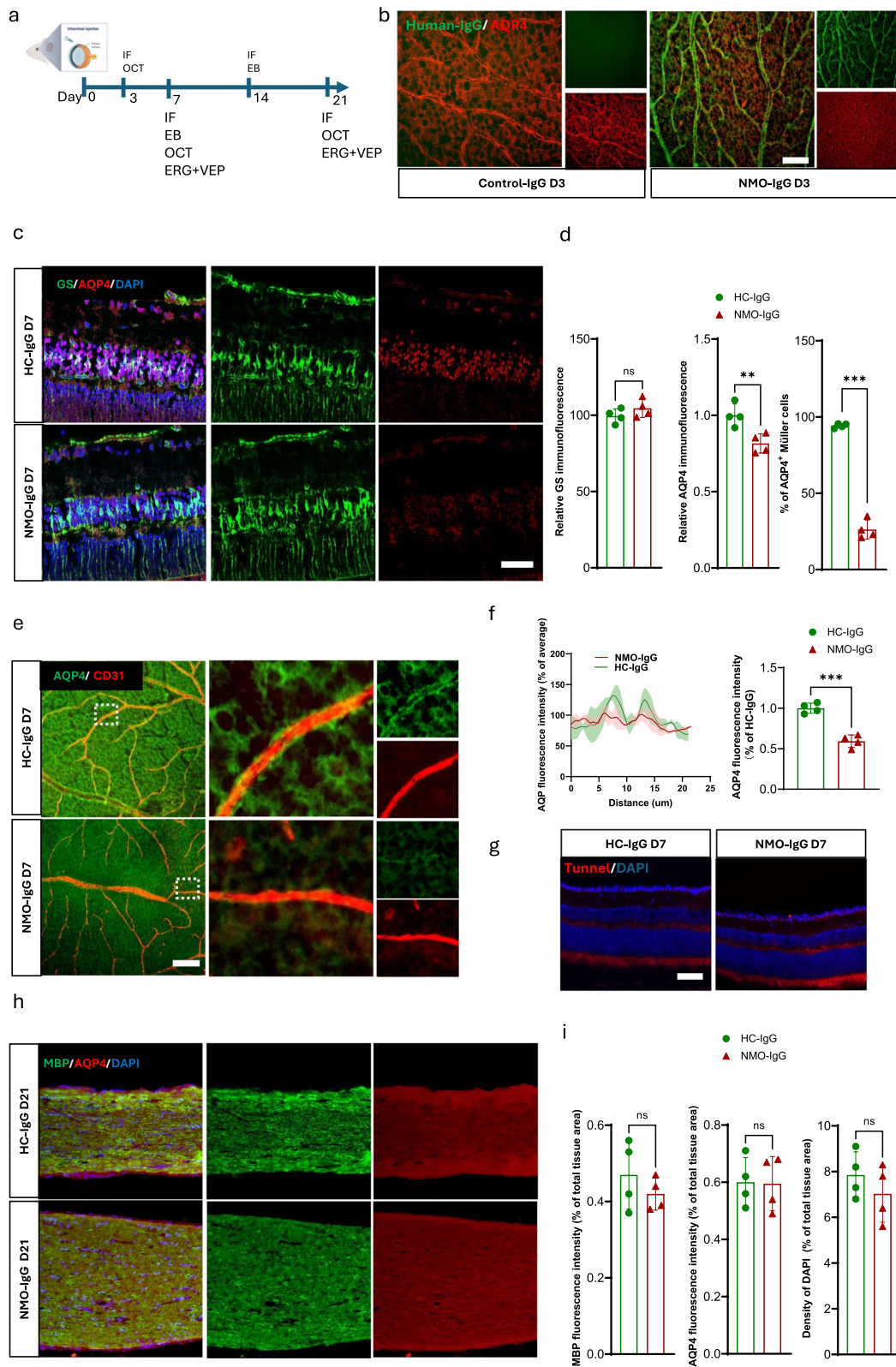


Fig. 1 (See legend on previous page.)

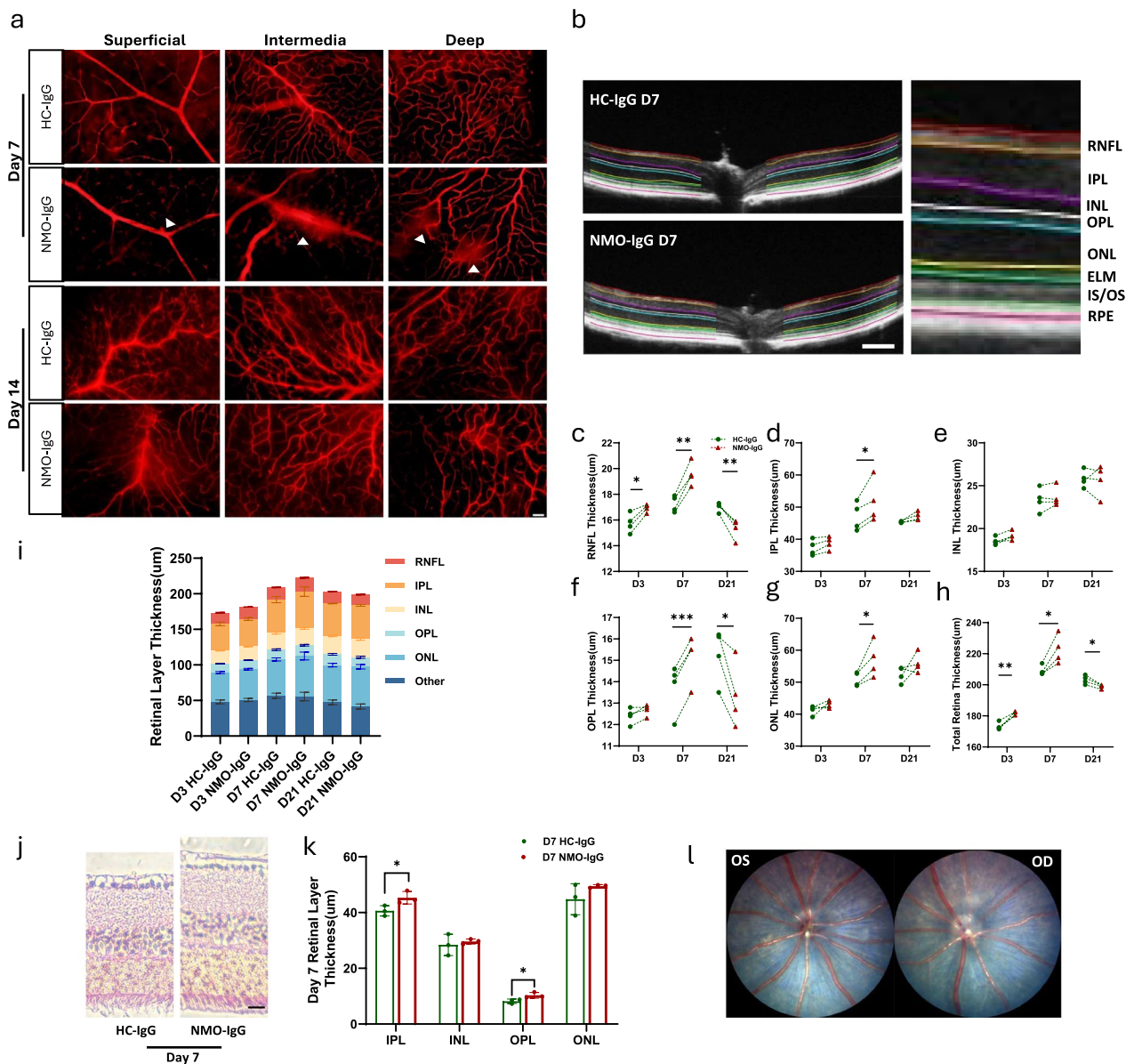


Fig. 2 NMO-IgG induces retinal vascular leakage and alterations in retinal layer thickness. **a** Visualization of the superficial, intermediate, and deep vascular plexuses using Evans Blue in retinal flat mounts. White arrows indicate areas of vascular leakage (Scale bar = 50 μ m). **b** Left: Representative retinal OCT images of retinal layers treated with HC-IgG (up) or NMO-IgG (down); Right: Schematic diagram illustrating the measurement of retinal layers. **c-h** Quantification of retinal layer thicknesses measured by OCT at different time points, including the RNFL, inner plexiform layer (IPL), inner nuclear layer (INL), outer plexiform layer (OPL), and outer nuclear layer (ONL). Dotted lines connect paired results from the same mouse (n = 4 per group). **i** Stacked column plots representing the thicknesses of various retinal layers. **j** H&E staining of the retina 7 days post-intravitreal injection (Scale bar: 10 μ m). **k** Quantification of IPL, INL, OPL, and ONL thicknesses in H&E-stained retinal sections (n = 3 per group). **l** Representative color fundus photographs showing the HC-IgG-treated eye (left OS) and the contralateral NMO-IgG-treated eye (right OD). * $p < 0.05$, ** $p < 0.01$, *** $p < 0.001$, t-test. Retinal thickness measurements were performed at intervals of 200 μ m from the optic nerve

GAPDH was used as a reference gene for normalization. Gene expression levels were calculated using the $2^{-\Delta\Delta CT}$ method.

Optical coherence tomography (OCT)

Retinal thickness was assessed using a retinal imaging system (isOCT 4D-ISOCT, Optoprobe, Burnaby, Canada). Mice were anesthetized, and their eyes were

dilated with 0.5% tropicamide eye drops. A single rectangular scan consisting of 800 A-scans by 800 B-scans over a $2.5 \times 2.5 \text{ mm}^2$ area centered on the optic nerve head (ONH) was performed on each eye. Retinal thickness was measured at 0.30 mm from the ONH. Images were acquired and retinal thickness measurements were calculated using software (version 2.0) from OptoProbe Research Ltd.

Electroretinogram (ERG) and flash visual evoked potential (f-VEP)

Mouse flash visual evoked potentials (f-VEP) and electroretinograms (ERG) were recorded using an OPTO-III visual electrophysiology instrument (Optoprobe Science, Burnaby, BC, Canada) to assess visual function. Mice were kept in darkness for over 12 h before the procedure, which was conducted under dim red light.

For ERG recording, a loop electrode was placed on the corneal surface of the eye being tested, while needle electrodes were inserted under the skin of the cheek and tail. For detecting flash VEPs, a needle electrode was inserted under the skin between the ears, replacing the loop electrode. Three stable waveforms were recorded for each eye (normal and injured) in each animal.

Dark-adapted 0.01 ERG, dark-adapted 3.0 ERG, light-adapted 3.0 ERG, and FVEP were recorded according to the international electrophysiological standard (ISCEV) (<http://www.iscev.org/standards>). The FVEP amplifier gain was 20 K with bandpass from 1 to 100 Hz. And 65 repeats were recorded. The dark-adapted 0.01 ERG and light-adapted 3.0 ERG amplifier gain were 4 K with bandpass from 1 to 100 Hz. The dark-adapted 3.0 ERG amplifier gain was 4 K with bandpass from 1 to 300 Hz. And 8 repeats were recorded in ERG.

Cell culture

MIO-M1 cells, an immortalized retinal Müller glial cell line, were obtained from Biopike Technology Company Ltd (Minnesota, USA) and cultured in Dulbecco's Modified Eagle Medium (DMEM) containing 4.5 g/l glucose, supplemented with 10% fetal bovine serum (FBS), 100 U/ml penicillin/streptomycin, and 1.0 mM glutamine.

BV2 microglia were obtained from Procell Life Science & Technology Co. Ltd (Wuhan, China) and cultured in

DMEM supplemented with 10% FBS and 100 U/ml penicillin/streptomycin. Both cell lines were maintained in a humidified incubator with 5% CO₂ at 37 °C. The culture medium was refreshed every 2–3 days until the cells reached confluency.

small-interfering RNA (siRNA) knockdown of AQP4

Three siRNA sequences targeting human AQP4 were designed and synthesized by Hanheng Biological Co. Ltd (Shanghai, China). Non-targeting siRNA was used as a control (NC). The siRNA sequence with the highest silencing efficiency was selected for subsequent experiments (siAQP4 sequence: GGUUGAGUUGAUAAU CACATT, Control siRNA sequence: UUCUCCGAA CGUGUCACGUTT).

Transfection was carried out using the RNAiMAX transfection reagent (No. 13778075, Invitrogen) according to the manufacturer's instructions. MIO-M1 cells were seeded into a 6-well plate, and RNAiMAX reagent, along with 5 pmol siRNA, was diluted separately in Opti-MEM and then added to each well. Treatments were conducted 24 h post-transfection.

Transwell co-culture of retinal müller cells and microglia

To investigate the effects of activated Müller cells on retinal microglia, MIO-M1 cells (retinal Müller glial cells) and BV2 cells (microglia) were co-cultured using a Transwell system. MIO-M1 cells at 70% confluence ($1.5 \times 10^4 \text{ cell/cm}^2$) were seeded into the wells of a 24-well plate containing 600 µl of media, while BV2 cells at 30% confluence ($2 \times 10^4 \text{ cell/cm}^2$) were placed in the Transwell permeable support membrane inserts with 200 µl of media, featuring an 8 µm pore size (Corning, USA), positioned above the MIO-M1 cells. The MIO-M1 cells were exposed to either control IgG or purified human IgG from patients (diluted 1:50 in culture media) for a duration of three hours. Following treatment, the upper chamber containing BV2 cells was inserted into the corresponding well of the 24-well plate, allowing these microglial cells to co-culture with MIO-M1 for an additional period of 24 h without replacing the medium in which MIO-M1 was cultured. After this co-culture period, all cells were washed with PBS. Subsequently,

(See figure on next page.)

Fig. 3 RGC loss and visual impairment in the intravitreal injection model. **a** Representative images of retinal flat mounts showing RBPMS⁺ RGCs (green) in the HC-IgG and NMO-IgG groups on days 7 and 21. The panoramic view of the retina is presented on the top (Scale bar: 1 mm) with a higher magnification of the indicated region shown on the bottom (Scale bar = 100 µm). **b** Bar graph showing the number of RGCs per mm² in each group (n = 4 animals in each group). **c** Representative figure and quantification analysis of electroretinography (ERG) responses recorded on days 7 and 21. **d** Representative and quantification analysis of flash visual evoked potential (f-VEP) responses recorded on days 7 and 21.

* $p < 0.05$, ** $p < 0.01$, t-test

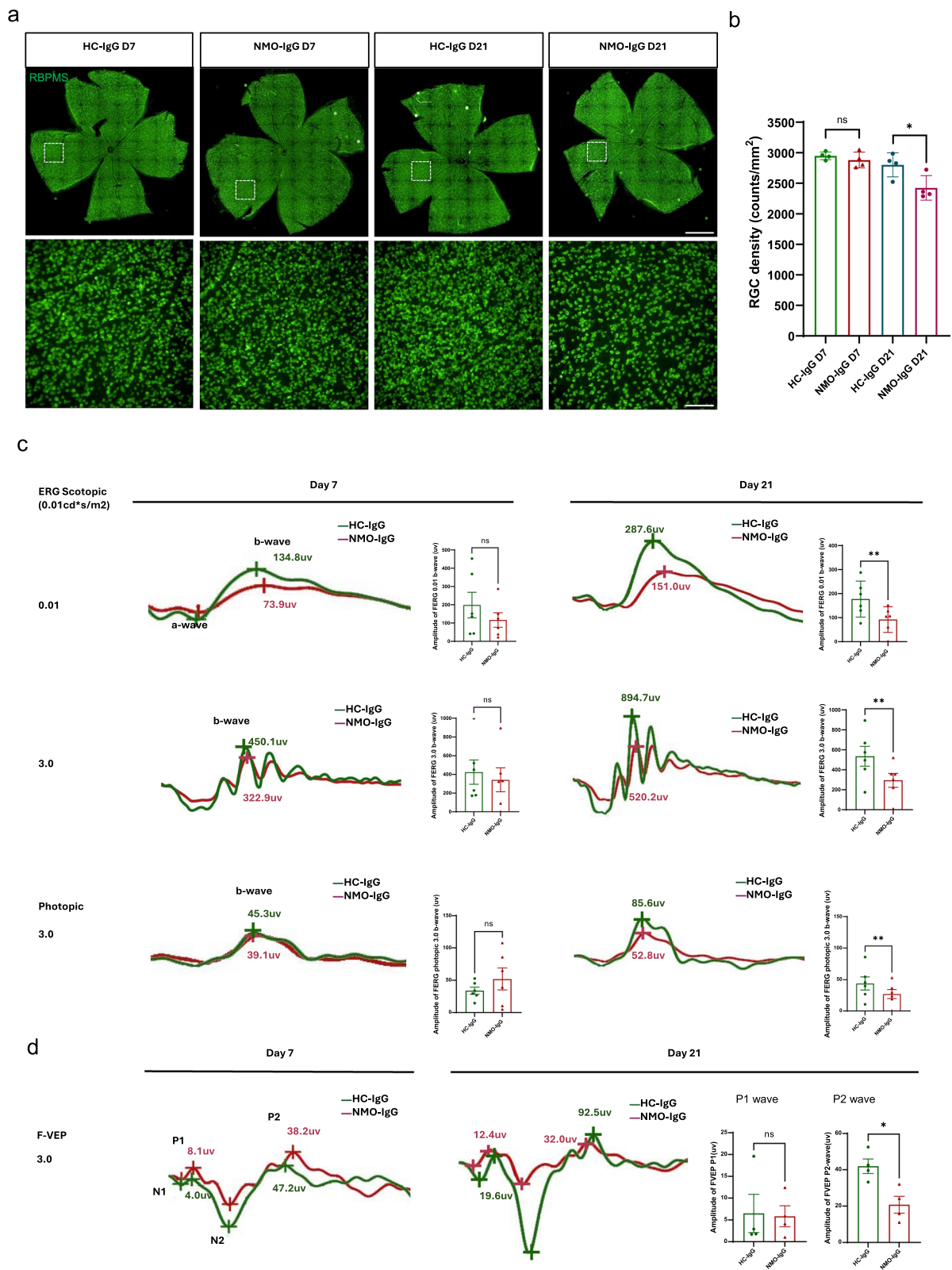


Fig. 3 (See legend on previous page.)

both MIO-M1 and BV2 cells were harvested for further mRNA analysis and immunofluorescent staining.

For the study involving AQP4 siRNA and NMO-IgG treatment, MIO-M1 cells were pretreated with AQP4 siRNA and a transfection reagent, followed by a recovery period of 48 h to allow for the degradation of the AQP4 protein.

Cell viability assay (CKK-8)

The cell viability was assessed using the Cell Counting Kit-8 (CKK-8, Dojindo Molecular Technologies, Japan) according to the manufacturer's instructions.

The BV2 cells were seeded in 96-well plates at a density of 1×10^6 cells per well and allowed to adhere overnight at 37 °C. Mouse C3/C3a (HY-P7863, MCE MedChem-Express Co., Ltd.) was subsequently added to the BV2 culture medium for a duration of 6 h. Following this incubation, the media were collected, and the concentration of C1qa was evaluated using an ELISA assay (E0747m, EIAab Science Inc., Wuhan, China).

Mouse primary retinal ganglion cells (RGCs) (CP-M122, Procell, Wuhan, China) were plated onto poly-L-lysine-coated plates and cultured in specialized RGC medium (CM-M122, Procell, Wuhan, China) at 37 °C within a standard cell incubator containing 5% CO₂ and 95% air. Prior to conducting cytotoxicity assays, mouse complement C1qa (HY-P71718, MCE MedChemExpress Co., Ltd.) was introduced into the culture medium until reaching a final concentration of 100 µg/ml. To neutralize C1qa activity effectively, ANX005 (HY-P990545, MCE MedChemExpress Co., Ltd.) was co-administered with C1qa at varying final concentrations of 5 µg/ml, 25 µg/ml, and 50 µg/ml, respectively. The RGCs were treated with either C1qa or the combination of C1qa + ANX005 for three hours; thereafter the culture media were replaced with specialized RGC medium and allowed to rest for ten minutes. Following this incubation period, 10 µl of

CKK-8 solution was added to each well before incubating the plates for four hours at 37 °C.

The absorbance at 450 nm was then measured using a SpectraMax® i3x Multi-Mode Microplate Reader (Molecular Devices). The absorbance values were directly proportional to the number of living cells, and cell viability was calculated as a percentage of the control group.

Statistical analysis

Quantitative data were normalized to the control group and presented as a percentage of the control (%). The normality tests were conducted using the Normality and Lognormality Tests available in Prism GraphPad software. The statistical significance of differences between groups was assessed through an independent sample t-test when comparing two groups. For comparisons involving more than two groups, one-way ANOVA was employed. If the data were not normally distributed, the Mann–Whitney rank-sum test was used instead. Statistical analyses and the generation of graphs were performed using GraphPad Prism 8.0 software (GraphPad Software Inc., San Diego, CA, USA). Statistical significance was indicated as follows: * $p < 0.05$; ** $p < 0.01$; *** $p < 0.001$.

Results

Intravitreal NMO-IgG induces AQP4 loss in the retina but not in the optic nerve

The experimental timeline is outlined in Fig. 1a. Following the intravitreal injection of NMO-IgG, no hemorrhages or signs of intraocular inflammation were detected under light microscopy. Three days post-injection, the binding of patient-derived NMO-IgG to retinal cells was examined. Immunofluorescence in retinal flat mounts, using a secondary antibody against human-IgG (green), revealed NMO-IgG deposition across the entire retina, particularly along blood vessels, where AQP4 was highly expressed in HC-IgG group (Fig. 1b). This pattern of NMO-IgG distribution aligns with previous studies [19,

(See figure on next page.)

Fig. 4 Microglial activation and RGC loss in response to NMO-IgG injection. **a** Representative images of retinal cryosections showing microglia (Iba1⁺ green) and iNOS⁺ cells (red) in the HC-IgG and NMO-IgG groups. Top: Merged images showed the retina layers and microglia (Scale bar = 20 µm); Middle: Enlarged image showed the co-localization of Iba1 and iNOS; Bottom: Signal channel of Iba1 and iNOS staining. **b** Bar graph displaying the number of Iba1⁺ cells per mm² in each group (n = 4 per group, 3 sections per eye). **c** Bar graph showing the number of Iba1⁺/iNOS⁺ cells per mm² in each group (n = 3 per group, 3 sections per eye). **d** Bar graph representing the iNOS mRNA levels in the retina on day 1 and day 7 after NMO-IgG injection (n = 3 per group). **e** Pie chart illustrating the percentage of iNOS⁺ cells among Iba1⁺ cells in the control-IgG and NMO-IgG-treated groups. **f** Representative image of microglia morphology indicated by Iba1 staining (green) in retinas treated by HC-IgG (top) or NMO-IgG (bottom). **g** Bar graph displaying the branch length of Iba1⁺ cells in each group (n = 4 per group, 3 sections per eye), (** $p < 0.01$). **h** Bar graph displaying the branch number of Iba1⁺ cells in each group (n = 4 per group, 3 sections per eye). **i** Curve of Iba1⁺ cell Sholl analysis in retinas treated by HC-IgG (green) or NMO-IgG (red). 25 cells per group. **j** Schematic timeline of PLX3397 treatment, IgG injection, and sample harvesting. **k** Left: Representative images of Iba1⁺ cells in retinas from normal diet or PLX3397 diet (Scale bar = 1 mm). Right: Higher magnification of the retina (Scale bar = 100 µm). **l** Visualization of retinal flat mounts showing RBPMs⁺ RGCs in the HC-IgG and NMO-IgG groups on days 7 and 21 with PLX3397 diet. The panoramic view is shown on the top (Scale bar = 1 mm) with a higher magnification of the indicated region displayed on the bottom (Scale bar = 100 µm). **m** Bar graph illustrating the number of RGCs per mm² in each group (n = 3 per group). ** $p < 0.01$; *** $p < 0.001$, t-test

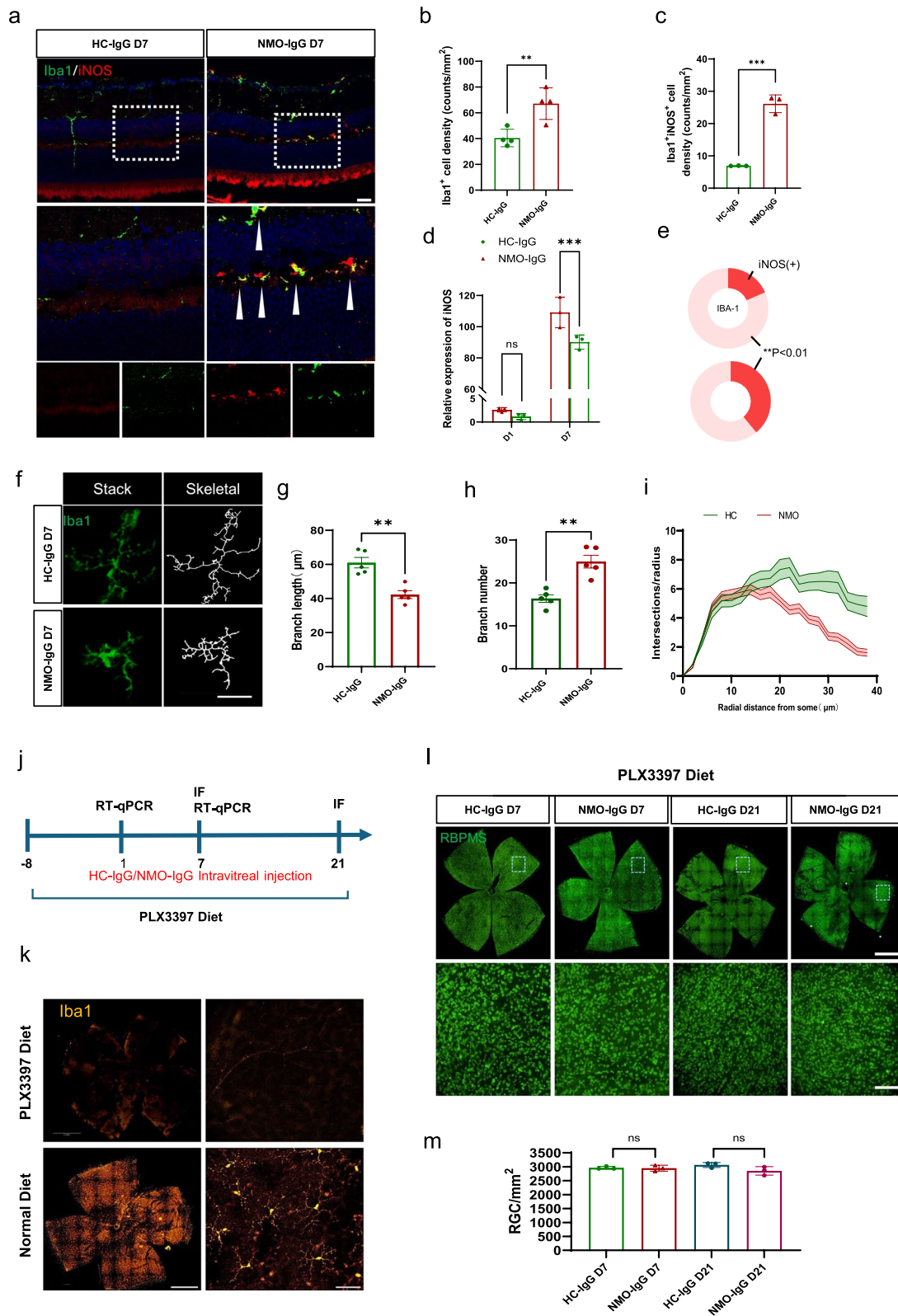


Fig. 4 (See legend on previous page.)

20]. Moreover, in HC-IgG group. No human IgG deposit was detected.

Further investigation using double immunofluorescent staining for AQP4 (red) and GS (green, a Müller cell marker) on cryosections of retinas treated with control-IgG showed that AQP4 is specifically expressed in Müller cells, which is consistent with an earlier study [21]. However, in retinas treated with NMO-IgG, a significant reduction in AQP4 expression was observed in Müller cells, without evidence of Müller cells loss (Fig. 1c, d, g).

In retinal flat mounts, double staining for AQP4 (green) and CD31 (red, an endothelial cell marker) confirmed that AQP4 was localized highly around blood vessels. The NMO-IgG treatment resulted in a noticeable loss of AQP4 in the perivascular region, as indicated by the line intensity profile of AQP4 and CD31 fluorescence (Fig. 1e, f).

Interestingly, despite the significant AQP4 loss in the retina, no such loss was observed in the optic nerves (Fig. 1h, i). Consistently, no myelination loss or cell density decrease in optic nerves in NMO-IgG treated group (Fig. 1h, i). This suggests that intravitreal injection of NMO-IgG does not penetrate the optic nerves, thereby not affecting AQP4 expression or induce demyelination in this region.

Intravitreal NMO-IgG produces retinal vascular leakage and alterations in retinal thickness

Given the significant deposition of NMO-IgG in the perivascular zone, we examined retinal blood vessel permeability in the presence or absence of NMO-IgG (Fig. 2a). Evans Blue dye was injected into the tail vein, and retinal flat mounts were examined on days 7 and 14 after human IgG administration. HC-IgG did not induce any blood vessel hyperpermeability on either day 7 or day 14. However, NMO-IgG caused significant leakage of retinal vessels on day 7, which partially recovered by day 14 but remained detectable in the superficial layers of a few samples (Fig. 2a).

AQP4 loss and blood leakage indicated abnormalities in water transport throughout the retina. We then investigated the effect of NMO-IgG on the thickness of the retinal layers. OCT images showed that, on day 7 after NMO-IgG injection, the total retinal thickness was substantially increased, particularly in the RNFL, IPL, and OPL (Fig. 2b–i). H&E staining of retinal sections also revealed similar results in the IPL and OPL (Fig. 2j, k). This altered thickness gradually reverted, with a significant decrease in RNFL thickness by day 21 (Fig. 2j, k). Notably, we did not observe papillary edema in any of the retinas throughout the study (Fig. 2l).

Intravitreal NMO-IgG contributes to RGC loss and visual dysfunction

The swelling of retinal layers indicated potential RGC injury in the NMO-IgG-treated group. To assess RGC loss, we performed immunofluorescent staining for the RGC-specific marker RBPMS on whole-mount retinas. There was no difference in RGC density between the NMO-IgG group and the control IgG group on day 7 after IgG injection, suggesting that NMO-IgG did not induce RGC injury at the early stage (Fig. 3a, b). However, by day 21, we observed a significant decrease in RGC density in the NMO-IgG group, indicating that the neuronal injury occurred at a relatively late stage (Fig. 3a, b).

We subsequently recorded electroretinography (ERG) and visual evoked potential (VEP) waveforms at various time points to assess retinal function. On day 7, the dark-adapted (scotopic) ERG revealed a slight reduction in b-wave amplitude while a-wave amplitude remained preserved in the NMO-IgG group compared to the control group, indicating minor retinal dysfunction. By day 21, both a-wave (data not shown) and b-wave amplitudes in light-adapted (photopic) and dark-adapted ERGs were significantly diminished, correlating with the retinal injury observed through staining techniques (Fig. 3c). Notably, previous research has demonstrated

(See figure on next page.)

Fig. 5 NMO-IgG mediates crosstalk between Müller cells and microglia in vivo. **a** Cumulative data showing mRNA level changes of C3 in retinas treated with NMO-IgG or HC-IgG. **b** Left: Representative image of dual fluorescence labeling for GS (green) and C3 (red) in retinas treated with NMO-IgG or HC-IgG; Middle: Enlarged images indicated detailed co-localization of GS and C3 in retina (white arrows); Right: Single channel image showed the GS and C3 staining (Scale bar = 20 μ m). **c** Bar graph showed the percentage of C3 + MIO-M1 cells in HC-IgG or NMO-IgG treated retinas (n = 4 per group, 3 sections per eye). **d** GS (red) and AQP4 (green) staining in MIO-M1 cells treated with PBS (top), HC-IgG (middle) or NMO-IgG (bottom) for 3 h (Scale bar = 20 μ m). **e** Left: Quantitative analysis of AQP4 average fluorescence intensity in each GS⁺ cell. Right: C3 mRNA expression level in MIO-M1 cells treated with PBS, HC-IgG, or NMO-IgG for 3 h. **f** Left: Representative images of Iba1 and iNOS in BV2 cells exposed to culture medium of MIO-M1 cells pretreated with PBS (top), HC-IgG (middle) or NMO-IgG (bottom); Right: the accompanying pie chart shows the ratio of iNOS⁺ Iba1⁺ microglia in each group. **g** Schematic of Transwell experiment. **h** Histograms display the AQP4 mRNA levels after control siRNA and AQP4 siRNA transfection. **i** Crystal violet staining showed the representative images of BV2 cells migration towards (Scale bar = 10 μ m). **j** Bar graph showed the numbers of BV2 cells migrating through the Transwell membrane **p* < 0.05, ***p* < 0.01, ****p* < 0.001. t-test (**a**, **c**, **h**) or One-Way ANOVA (**e**, **j**)

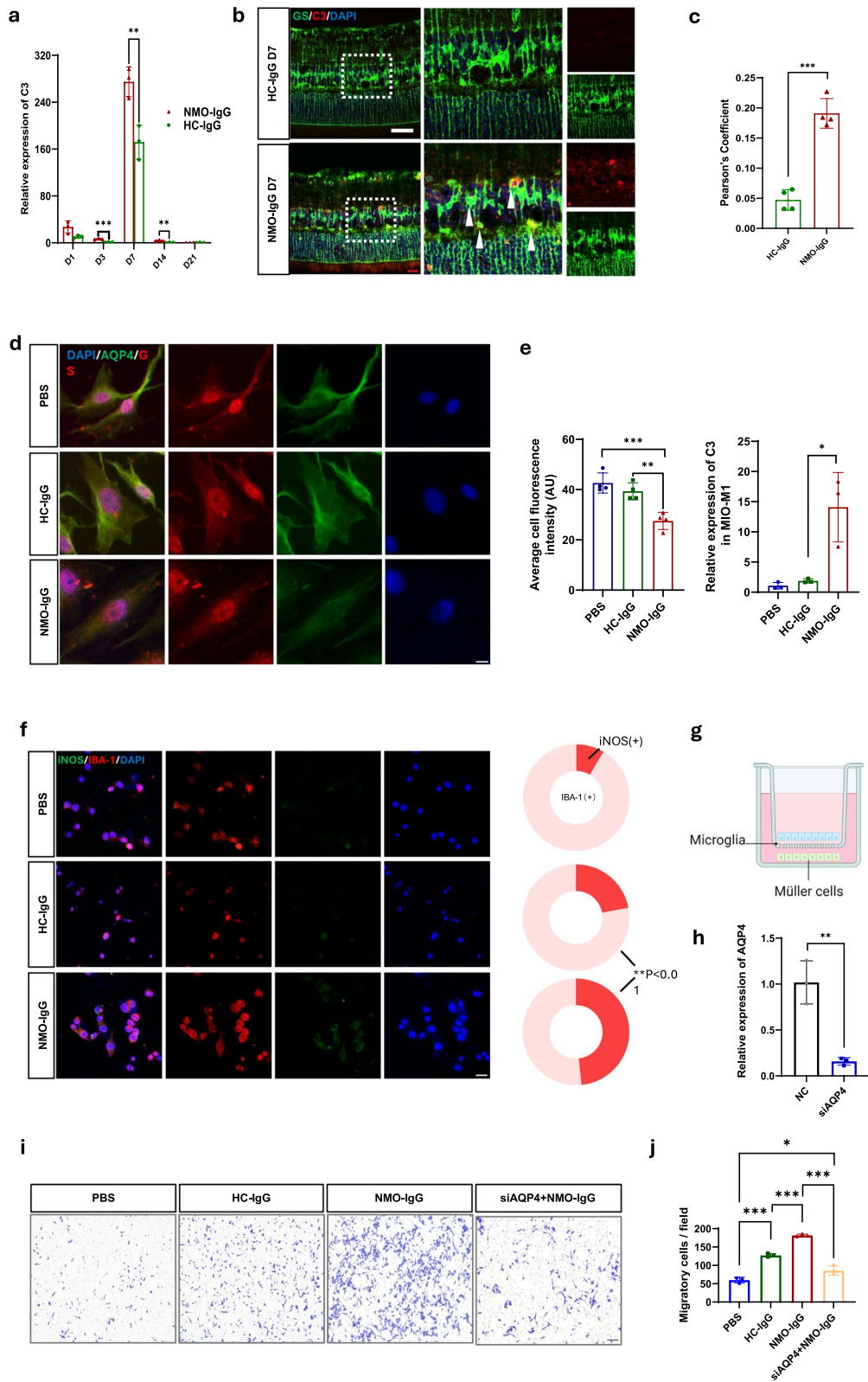


Fig. 5 (See legend on previous page.)

that Müller cell injury leads to abnormalities in the b wave [22, 23]. Furthermore, F-VEP results demonstrated a notable decrease in wave amplitude on day 21, confirming that NMO-IgG-dependent retinopathy subsequently affecting retinal ganglion cells (RGCs), as illustrated in Fig. 3d.

Microglial inflammation contributes to NMO-IgG-induced retinopathy

The swelling of retinal layers and dysfunction of RGCs indicated potential inflammation in the retina after NMO-IgG injection. Given that microglia are the primary immune cells in the retina, we hypothesized their critical role in NMO-IgG-induced retinopathy. Iba1 immunostaining revealed significant microgliosis following NMO-IgG injection. Furthermore, mRNA analysis showed that iNOS, a inflammatory microglia marker [24], significantly increased, suggesting an inflammatory role for microglia (Fig. 4a–e). Microglia Sholl analysis indicated that in NMO-IgG treated retina, microglia have more branch numbers and shorter branch length (Fig. 4f–i), which is consistent with the microglia morphology change in spinal cord NMO model [12].

To confirm the contribution of inflammatory microglia to neuronal injury in the NMO-IgG-treated retina, we performed microglia depletion using the CSF1 receptor antagonist PLX3397 (Fig. 4j). Iba1 immunostaining demonstrated that microglia were completely ablated after 7 days of feeding with PLX3397 chow (Fig. 4k). Consistently, microglial ablation significantly reduced NMO-IgG-induced RGC loss, suggesting that microglial suppression may provide protection against retinal ganglion cell loss following NMO-IgG transfer (Fig. 4l, m).

Müller cell-derived complement C3 activates microglia following NMO-IgG-induced AQP4 internalization

In previous studies, we reported that NMO-IgG induces AQP4 internalization and upregulates complement C3 expression in astrocytes [12, 13]. To further investigate this process in the retina, we examined complement C3 expression in the NMO-IgG intravitreal injection

model. RT-qPCR analysis over a 21-day period revealed that C3 expression peaked on day 7 post-injection and then gradually decreased (Fig. 5a). Consistently, immunofluorescence staining showed clear co-localization of GS and C3 on day 7 after NMO-IgG injection, indicating that NMO-IgG administration on Müller cells led to increased complement C3 production (Fig. 5b, c).

Given that complement C3-activated microglia induce evolving NMO lesions in the spinal cord [12], we hypothesized that retinal microglia might be activated by Müller cell-derived C3. To test this, we treated the Müller cell line MIO-M1 with NMO-IgG and examined AQP4 expression. Consistent with the in vivo model, AQP4 staining quantification showed a dramatic decrease 24 h after NMO-IgG treatment (Fig. 5d, e). Complement C3 mRNA expression was significantly elevated in MIO-M1 cells treated with NMO-IgG compared to the PBS and HC-IgG groups (Fig. 5e).

Additionally, we treated MIO-M1 cells with NMO-IgG then remove the autoantibodies, and then put BV2 cell containing transwells in the MIO-M1 culture dish (Fig. 5g). The NMO-IgG pretreatment induced robust BV2 cell migration compared to HC-IgG group (Fig. 5i). This NMO-IgG-dependent Müller cell-microglia communication also increased iNOS expression in BV2 cells, indicating an inflammatory response (Fig. 5f). To confirm that Müller cell-microglia communication was AQP4-IgG-specific, we transfected AQP4 siRNA into MIO-M1 cells to downregulate AQP4 expression. The AQP4 siRNA effectively reduced AQP4 mRNA expression in MIO-M1 cells (Fig. 5h), which also alleviated NMO-IgG-induced microglia migration in MIO-M1/BV2 co-cultures (Fig. 5i, j).

C1q derived from activated microglia is neurotoxic to RGCs in NMO-IgG-induced retinopathy

The complement pathway initiator C1q is primarily released by activated microglia. In the retina treated

(See figure on next page.)

Fig. 6 Microglial C1q contributes to neuronal injury in NMO-IgG-induced RGC injury. **a** mRNA levels of C1q in retinas treated with NMO-IgG or HC-IgG (n = 4 per group). **b** Representative image of immunofluorescence staining showing C1q expression in microglia (Iba1⁺ cells) within the retina treated with NMO-IgG or HC-IgG (n = 4 per group). **c** Pie graph of the percentage of C1q⁺ microglia (n = 3 per group). **d** Bar graph showed the C1q⁺ microglia numbers in retina treated with NMO-IgG or HC-IgG (n = 3 per group). **e** Bar graph of C1q mRNA level in retina treated with normal diet or PLX3397 diet (n = 3 per group). **f** Bar graph of C3 mRNA level in retina treated with normal diet or PLX3397 diet (n = 3 per group). **g** PLX3397 inhibits NMO-IgG-induced C1q expression but did not change retina C3 expression in NMO-IgG treated retina (n = 3 per group). **h** Bar graph shows the C1q concentration in the culture medium of BV2 cells treated with mouse complement C3 (n = 4 per group). **i** CCK8 assay shows the cell viability of primary RGCs treated with PBS or C1q. C1q induced significant cell damage as measured by CCK8 assay (n = 4 per group). **j** ANX005 reduces C1q-induced RGCs injury in a dose-dependent manner (n = 4 per group). **p* < 0.05, ***p* < 0.01, ****p* < 0.001. t-test (**a, c–g, i**) or One-Way ANOVA (**h, j**)

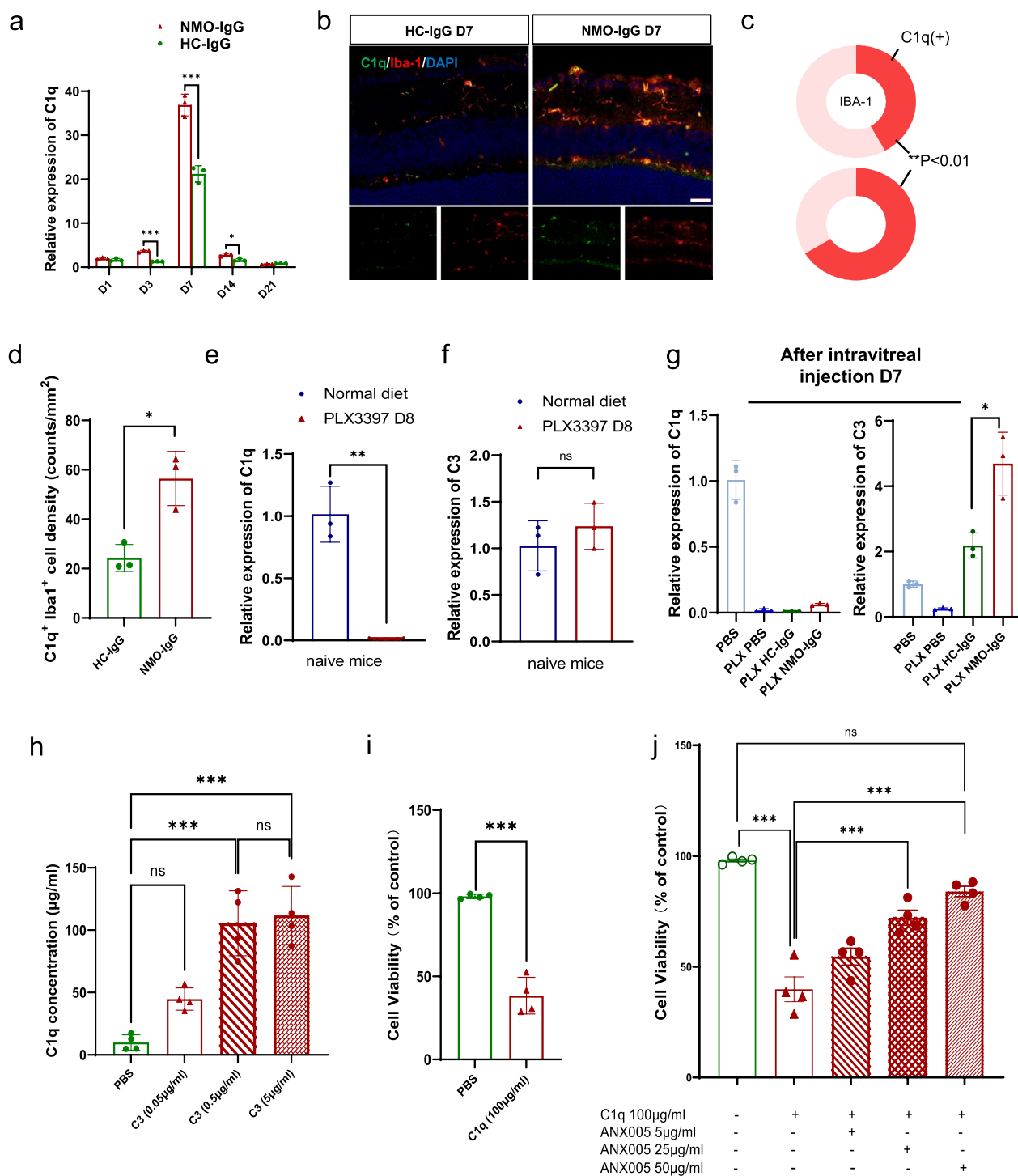


Fig. 6 (See legend on previous page.)

with NMO-IgG, C1q mRNA levels significantly increased by day 7 (Fig. 6a). We also observed C1q protein within microglia located in the NMO-IgG-induced retinal lesion (Fig. 6b–d). Remarkably, the depletion of microglia using PLX3397 completely

inhibited NMO-IgG-induced C1q expression (Fig. 6e). However, this depletion did not affect the expression of complement C3 (Fig. 6f, g), which is produced by Müller cells.

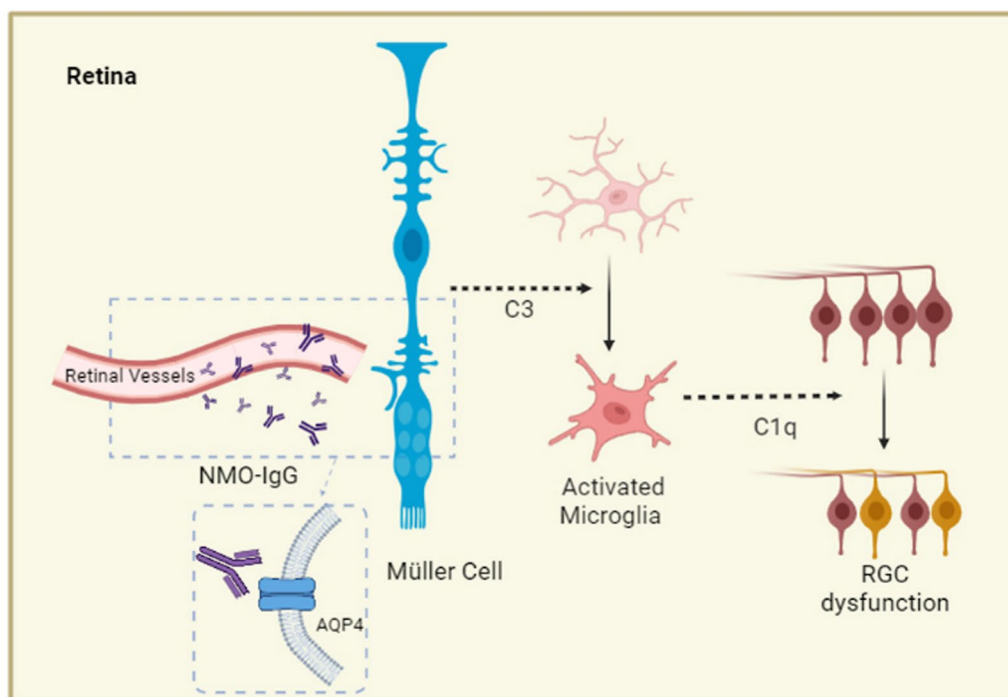


Fig. 7 Microglial C1q mediated retinopathy in NMO-IgG-induced retinopathy

To further investigate the role of C1q in retinal neurotoxicity, we explored whether C1q alone could induce neurotoxicity in a cell culture model. When BV2 cells were treated with mouse complement C3 for 6 h, the C1qa concentration in medium was increased (Fig. 6h), the C3a induced C1q production is concentration sensitive, which reached the peak at a concentration of 5 $\mu\text{g/ml}$. while the maximum C1q production is around 100 $\mu\text{g/ml}$ (Fig. 6h). When primary cultured mouse RGCs were treated with 100 $\mu\text{g/ml}$ of mouse C1qa, significant RGC damage was observed, as measured by the CCK8 assay (Fig. 6i). Additionally, the C1q-neutralizing antibody ANX005 reduced C1q-induced RGCs injury in a dose-dependent manner (Fig. 6h).

Discussion

Clinical evidence suggests that AQP4-IgG seropositive NMOSD patients without a clinical history of optic neuritis (ON) exhibit lower macular RNFL and GCIPL thickness and faster rates of peripapillary RNFL (pRNFL) thinning compared to healthy controls [25]. Foveal thickness is also reduced in NMOSD patients who have not experienced visual symptoms [26]. However, another cohort study revealed that while macular outer plexiform layer (OPL) and outer nuclear layer (ONL) loss was not specific to AQP4-IgG seropositive NMOSD, reductions

in the RNFL and ganglion cell-inner plexiform layer (GCIPL) were still observed [27].

These clinical findings raise the question of whether primary retinopathy exists in NMOSD [28]. Clinically, it is challenging to rule out the presence of possible asymptomatic subclinical optic nerve lesions and trans-synaptic degeneration in the affected eyes. Mechanistically, AQP4 is polarized in the membrane domains of astrocytes and Müller cells, which face the vitreous body and blood vessels in the retina [29]. It is possible that NMO-IgG increases vascular permeability, promoting its transferability and allowing it to penetrate deep into the retina, cross the blood-retinal barrier, and bind to AQP4. Therefore, clinical evidence of AQP4-IgG in intraocular fluid (aqueous humor and vitreous liquid) remains necessary to understand the impaired retinal homeostatic mechanisms in NMOSD.

The passive transfer of AQP4-IgG into the central nervous system via intrathecal, intravenous, and intracranial injection has been shown to induce NMO-like pathology [12, 30, 31]. While ON and myelitis are potential outcomes of these models, their impact on the retina is limited. A 2016 study by Felix et al. reported that intravitreal injection of rAb-53 in a rat model demonstrated that AQP4-IgG can cause primary RGC loss and thinning of the ganglion cell complex through a complement-independent pathway [20]. Zeka et al. found that AQP4 loss in Müller cells correlated with T cell infiltration and

microglia activation/macrophage recruitment but not with antibody-dependent cellular cytotoxicity (ADCC) or CDC [30, 31].

In our study, we developed a new intravitreal injection mouse model without exogenous complement to further explore retinopathy. A clinical study revealed that in NMO patients, the complement cascade mediated cell death makes no difference to the disease onset and recovery phase [32]. In addition, human NMO-IgG has limited ability to activate the mouse complement system [33]. Therefore, we hypothesized that pathology and functional impairment are not induced by CDC. Our observations revealed significant AQP4 loss in NMO-IgG-treated retinas without evidence of Müller cell death. This finding contradicts the idea of Müller cell apoptosis and supports the notion of AQP4 internalization following IgG binding [29]. NMO-IgG-induced AQP4 internalization could potentially reduce complement deposition on the cell surface, thereby protecting Müller cells from CDC [10].

Microglia activation is another significant pathological feature observed in our experimental mice. Microglia activity was also reported in a rat model of AQP4-IgG induced optic neuritis model [34]. We previously demonstrated that in a mouse NMO spinal cord model, astrocytic C3 activates microglia via microglial C3a receptors [12, 13]. The C3-C3aR pathway, which mediates microglia-astrocyte interaction, has recently been described in demyelinating diseases and neurodegenerative disorders [12, 13]. The upregulation of C3, specifically associated with neurotoxicity in both the retina and spinal cord, drives microglia to release pro-inflammatory cytokines [35]. Consistently, in the retina, NMO-IgG induced complement C3 expression in Müller cells, leading to microglia-Müller cell interaction [14].

This microglia-Müller cell interaction coincided with significant RGC loss and BRB hyperpermeability following NMO-IgG treatment. The observed RNFL thinning and INL thickening in this model align with findings from our previous clinical study [5]. Specifically, our prior work showed that individuals positive for AQP4-IgG antibodies had thinner peripapillary RNFL and thicker INL compared to those negative for the antibodies [36, 37]. The fluctuation in inner retinal layer thickness in this model may be associated with the loss of perivascular AQP4 and subsequent vascular leakage. Previous studies have reported subclinical changes in parafoveal vessels, suggesting that the intermediate vascular plexus in the INL and the deep vascular plexus in the ONL could be involved at an early stage of NMOSD [36, 38].

Although C3-expressing astrocytes have been reported to be neurotoxic [39], our study suggests that microglia activation is crucial in NMO-IgG-induced retinopathy.

Microglia ablation prevented NMO-IgG-induced neuronal damage, indicating that the interaction between activated microglia and Müller cells plays a central role in retinal injury. On the other hand, reactive microglia produce IL-1 α , TNF, and C1q, which can sufficiently induce the A1 astrocyte phenotype [40, 41]. Astrocyte dysfunction results in downregulation of chemokines and growth factors which maintain the homeostasis of the central nervous system [42, 43]. Notably, in our model, C3 expression in the non-ablated group was much higher than in the microglia-ablated group, suggesting a positive feedback loop between activated microglia and Müller cells.

Activated microglia upregulated complement C1q, the initial complement protein [44]. C1q has been reported to bind to mitochondria, block the respiratory chain, and induce neuronal oxidative stress [45]. Additionally, C1q can bind to endothelial cells, leading to BRB hyperpermeability [46]. Therefore, microglial C1q might induce RGC cell loss and retinal vessel leakage in this model (Fig. 7).

Another pathological observation in our study is that NMO-IgG induced Müller cell dysfunction. As part of the retinal neurovascular unit, Müller cells are essential for maintaining retinal homeostasis and regulating the progression of retinal inflammation [19, 47]. The binding of autoantibodies to AQP4 mediates partial AQP4 internalization before complement cascade initiation, leading to reduced plasma membrane water permeability. This impairment in cell volume regulation results in adverse swelling under stressful conditions in the retina. Another study showed that in AQP4^{-/-} mice, a sustained thickening of the retina, primarily due to changes in the inner retinal layers, was observed during recovery from experimental autoimmune encephalomyelitis (EAE) [47–49]. Subsequently, this thickening dropped below its baseline level. Müller cell dysfunction in AQP4^{-/-} mice results in structural damage to the gliovascular unit of the retina and promotes scar formation during CNS inflammation [47]. Therefore, we propose that the thickness changes in the intravitreal NMO-IgG infusion model are mainly driven by Müller cells (Fig. 7).

There are still several limitations to our experiments. First, the long-term effects of NMO-IgG in the retina remain unclear. Further evaluation and observation over an extended period, along with detailed pathological studies, are required. Additionally, our experimental results, such as the *in vivo* expression levels of C3, cannot definitively rule out the contribution of astrocytes. Furthermore, C3aR (complement C3a receptor) antagonists and C3aR knockout mice should be utilized in future research to further elucidate the mechanisms underlying Müller cell-microglia interaction. The

pathogenesis of retinal abnormalities in NMO/D may be multifactorial and more complex than a simple pathogenic role of NMO-IgG, warranting further investigation.

In conclusion, NMO-IgG induces primary retinopathy through a complement-independent pathway, with microglia activation playing a critical role in NMO pathogenesis. Müller cell-derived C3 is an upstream factor in microglial C1q release, and restricting microglia activation could be a novel therapeutic target for NMO-IgG-induced retinopathy.

Abbreviations

NMO	Neuromyelitis optica
AQP4	Aquaporin-4
GFAP	Glial fibrillary acidic protein
GS	Glutamine synthetase
Iba1	Ionized calcium-binding adaptor molecule-1
RBPM5	RNA-binding protein with multiple splicing
OCT	Optical coherence tomography
ERG	Electroretinography
f-VEP	Flash visual evoked potential
RT-qPCR	Real-time fluorescence quantitative PCR
CSF1R	Colony stimulating factor 1 receptor
Arg-1	Arginase-1
iNOS	Inducible nitric oxide synthase
PFA	Paraformaldehyde
H&E	Hematoxylin and eosin
RNFL	Retinal nerve fiber layer
SD-OCT	Spectral-domain optical coherence tomography
RGCs	Retinal ganglion cells
INL	Inner nuclear layer
IPL	Inner plexiform layer
ONL	Outer nuclear layer
OPL	Outer plexiform layer
DMEM	Dulbecco's modified eagle medium
FBS	Fetal bovine serum

Acknowledgements

I would like to express my deepest gratitude to Prof. Kwok Fai So for his invaluable guidance and support in the establishment of the lab. His expertise, insights, and unwavering encouragement have been essential throughout this journey. My heartfelt thanks also go to Prof. Erdan Dong, Prof. Hong Jiang, Prof. Qiji Liu, Dr. Qingjie Mu for their tireless help and contributions. Their dedication, teamwork, and invaluable assistance have made this project possible, and I am deeply appreciative of their constant support.

Author contributions

T.C. and S.W. conceived the study and coordinated the project. B.C. and H.Z. designed the experiments. B.C., H.S.M.S., W.Y., Q.L.K.Y. and M.S. performed the experiment. Q.X., W.Y., and Y.L. analyzed the data. Y.Y., Q.L. and M.G. reviewed the manuscript. All authors read and approved the final manuscript.

Funding

This project was supported by the National Natural Science Foundation of China, under grant No. 82471377, awarded to Tingjun Chen, and the Qingdao Natural Science Foundation, under grant No. 23-2-1-169-zyyd-jch awarded to Tingjun Chen. Additionally, this project also received support from National Key Research and Development Program of China, under Grant NO. 2022YFA1105503 awarded to Shihui Wei.

Availability of data and materials

No datasets were generated or analysed during the current study.

Declarations

Ethics approval and consent to participate

All experimental procedures described in this article were reviewed and approved by the Ethics Committee of Chinese PLA General Hospital.

Consent for publication

Not applicable.

Competing interests

The authors declare no competing interests.

Author details

¹Department of Ophthalmology, the Third Medical Center of Chinese People's Liberation, Army General Hospital, Beijing 100853, People's Republic of China.

²The Chinese People's Liberation Army Medical School, Beijing, People's Republic of China. ³State Key Laboratory of Kidney Diseases, General Hospital of Chinese People's Liberation Army, Beijing, People's Republic of China.

⁴Department of Ophthalmology, Bethune International Peace Hospital, Shijiazhuang, Hebei, China. ⁵College of Health and Life Science, University of Health and Rehabilitation Sciences, Qingdao, Shandong, People's Republic of China. ⁶Department of Ophthalmology, Qingdao Municipal Hospital, University of Health and Rehabilitation Sciences, Qingdao, Shandong, People's Republic of China. ⁷College of Veterinary Medicine, Qingdao Agricultural University, Qingdao, Shandong, People's Republic of China.

Received: 1 September 2024 Accepted: 14 February 2025

Published online: 07 March 2025

References

1. Asgari N, Lillevang ST, Skejoe HPB, Kyvik KO. Epidemiology of neuromyelitis optica spectrum disorder in Denmark (1998–2008, 2007–2014). *Brain Behav.* 2019;9:e01338.
2. Jonsson DI, Sveinsson O, Hakim R, Brundin L. Epidemiology of NMO/D in Sweden from 1987 to 2013: a nationwide population-based study. *Neurology.* 2019;93:e181–9.
3. Jarius S, Paul F, Weinschenker BG, Levy M, Kim HJ, Wildemann B. Neuromyelitis optica. *Nat Rev Dis Primers.* 2020;6:85.
4. Peng A, Qiu X, Zhang L, Zhu X, He S, Lai W, Chen L. Evaluation of the retinal nerve fiber layer in neuromyelitis optica spectrum disorders: a systematic review and meta-analysis. *J Neurol Sci.* 2017;383:108–13.
5. Peng CX, Li HY, Wang W, Wang JQ, Wang L, Xu QG, Cao SS, Zhou HF, Zhao S, Wei SH. Retinal segmented layers with strong aquaporin-4 expression suffered more injuries in neuromyelitis optica spectrum disorders compared with optic neuritis with aquaporin-4 antibody seronegativity detected by optical coherence tomography. *Br J Ophthalmol.* 2017;101:1032–7.
6. Lennon VA, Kryzer TJ, Pittock SJ, Verkman AS, Hinson SR. IgG marker of optic-spinal multiple sclerosis binds to the aquaporin-4 water channel. *J Exp Med.* 2005;202:473–7.
7. Saadoun S, Waters P, Bell BA, Vincent A, Verkman AS, Papadopoulos MC. Intra-cerebral injection of neuromyelitis optica immunoglobulin G and human complement produces neuromyelitis optica lesions in mice. *Brain.* 2010;133:349–61.
8. Hinson SR, Clift IC, Luo N, Kryzer TJ, Lennon VA. Autoantibody-induced internalization of CNS AQP4 water channel and EAAT2 glutamate transporter requires astrocytic Fc receptor. *Proc Natl Acad Sci USA.* 2017;114:5491–6.
9. Howe CL, Kaptzan T, Magana SM, Ayers-Ringler JR, LaFrance-Corey RG, Lucchinetti CF. Neuromyelitis optica IgG stimulates an immunological response in rat astrocyte cultures. *Glia.* 2014;62:692–708.
10. Tradtrantip L, Yeaman MR, Verkman AS. Cytoprotective IgG antibodies in sera from a subset of patients with AQP4-IgG seropositive neuromyelitis optica spectrum disorder. *Sci Rep.* 2021;11:21962.
11. Guo Y, Lennon VA, Parisi JE, Popescu B, Vasquez C, Pittock SJ, Howe CL, Lucchinetti CF. Spectrum of sublytic astrocytopathy in neuromyelitis optica. *Brain.* 2022;145:1379–90.

12. Chen T, Lennon VA, Liu YU, Bosco DB, Li Y, Yi MH, Zhu J, Wei S, Wu LJ. Astrocyte-microglia interaction drives evolving neuromyelitis optica lesion. *J Clin Invest.* 2020;130:4025–38.
13. Chen T, Bosco DB, Ying Y, Tian DS, Wu LJ. The emerging role of microglia in neuromyelitis optica. *Front Immunol.* 2021;12:616301.
14. Xu L, Xu H, Chen S, Jiang W, Afridi SK, Wang Y, Ren X, Zhao Y, Lai S, Qiu X, et al. Inhibition of complement C3 signaling ameliorates locomotor and visual dysfunction in autoimmune inflammatory diseases. *Mol Ther.* 2023;31:2715–33.
15. Zhang W, Han Y, Huang H, Su Y, Ren H, Qi C, Li J, Yang H, Xu J, Chang G, et al. CD22 blockade exacerbates neuroinflammation in Neuromyelitis optica spectrum disorder. *J Neuroinflamm.* 2024;21:313.
16. Tomita Y, Qiu C, Bull E, Allen W, Kotoda Y, Talukdar S, Smith LEH, Fu Z. Muller glial responses compensate for degenerating photoreceptors in retinitis pigmentosa. *Exp Mol Med.* 2021;53:1748–58.
17. Wingerchuk DM, Banwell B, Bennett JL, Cabre P, Carroll W, Chitnis T, de Seze J, Fujihara K, Greenberg B, Jacob A, et al. International consensus diagnostic criteria for neuromyelitis optica spectrum disorders. *Neurology.* 2015;85:177–89.
18. Bolte S, Cordelieres FP. A guided tour into subcellular colocalization analysis in light microscopy. *J Microsc.* 2006;224:213–32.
19. Nicchia GP, Pisani F, Simone L, Cibelli A, Mola MG, Dal Monte M, Frigeri A, Bagnoli P, Svelto M. Glio-vascular modifications caused by Aquaporin-4 deletion in the mouse retina. *Exp Eye Res.* 2016;146:259–68.
20. Felix CM, Levin MH, Verkman AS. Complement-independent retinal pathology produced by intravitreal injection of neuromyelitis optica immunoglobulin G. *J Neuroinflamm.* 2016;13:275.
21. Han C, Li Y, Zheng X, Zhang X, Li G, Zhao L, Chen Z, Yang Y, Zhang W. AQP4- and Kir4.1-mediated muller cell oedema is involved in retinal injury induced by hypobaric hypoxia. *Mol Neurobiol.* 2024;62:2012.
22. Szamier RB, Ripps H, Chappell RL. Changes in ERG b-wave and Muller cell structure induced by alpha-aminoadipic acid. *Neurosci Lett.* 1981;21:307–12.
23. You Y, Zhu L, Zhang T, Shen T, Fontes A, Yiannikas C, Parratt J, Barton J, Schulz A, Gupta V, et al. Evidence of muller glial dysfunction in patients with aquaporin-4 immunoglobulin G-positive neuromyelitis optica spectrum disorder. *Ophthalmology.* 2019;126:801–10.
24. Paolicelli RC, Sierra A, Stevens B, Tremblay ME, Aguzzi A, Ajami B, Amit I, Audinat E, Bechmann I, Bennett M, et al. Microglia states and nomenclature: a field at its crossroads. *Neuron.* 2022;110:3458–83.
25. Kim NH, Kim HJ, Park CY, Jeong KS, Cho JY. Optical coherence tomography versus visual evoked potentials for detecting visual pathway abnormalities in patients with neuromyelitis optica spectrum disorder. *J Clin Neurol.* 2018;14:200–5.
26. Tiftikcioglu BI, Emre S, Idiman F, Idiman E. Optical coherence tomography angiography (OCTA) in differential diagnosis of aquaporin-4 antibody seronegative NMOSD and multiple sclerosis. *Mult Scler Relat Disord.* 2022;58: 103503.
27. Zhang X, Xiao H, Liu C, Zhao L, Wang J, Li H, Wang R, Zhu Y, Chen C, Wu X, et al. Comparison of macular structural and vascular changes in neuromyelitis optica spectrum disorder and primary open angle glaucoma: a cross-sectional study. *Br J Ophthalmol.* 2021;105:354–60.
28. Filippatou AG, Vasileiou ES, He Y, Fitzgerald KC, Kalaitzidis G, Lambe J, Mealy MA, Levy M, Liu Y, Prince JL, et al. Optic neuritis-independent retinal atrophy in neuromyelitis optica spectrum disorder. *J Neuroophthalmol.* 2022;42:e40–7.
29. Netti V, Fernandez J, Melamud L, Garcia-Miranda P, Di Giusto G, Ford P, Echevarria M, Capurro C. Aquaporin-4 removal from the plasma membrane of human muller cells by AQP4-IgG from patients with neuromyelitis optica induces changes in cell volume homeostasis: the first step of retinal injury? *Mol Neurobiol.* 2021;58:178–93.
30. Zeka B, Hastermann M, Kaufmann N, Schanda K, Pende M, Misu T, Rommer P, Fujihara K, Nakashima I, Dahle C, et al. Aquaporin 4-specific T cells and NMO-IgG cause primary retinal damage in experimental NMO/SD. *Acta Neuropathol Commun.* 2016;4:82.
31. Zeka B, Lassmann H, Bradi M. Muller cells and retinal axons can be primary targets in experimental neuromyelitis optica spectrum disorder. *Clin Exp Neuroimmunol.* 2017;8:3–7.
32. Jitraprakulsan J, Fryer JP, Majed M, Smith CY, Jenkins SM, Cabre P, Hinson SR, Weinschenker BG, Mandrekar J, Chen JJ, et al. Clinical utility of AQP4-IgG titers and measures of complement-mediated cell killing in NMOSD. *Neurol Neuroimmunol Neuroinflamm.* 2020;7:e727.
33. Moinfar Z, Zamvil SS. Microglia complement astrocytes in neuromyelitis optica. *J Clin Invest.* 2020;130:3961–4.
34. Morita Y, Itokazu T, Nakanishi T, Hiraga SI, Yamashita T. A novel aquaporin-4-associated optic neuritis rat model with severe pathological and functional manifestations. *J Neuroinflamm.* 2022;19:263.
35. Zhang LY, Pan J, Mamtilahun M, Zhu Y, Wang L, Venkatesh A, Shi R, Tu X, Jin K, Wang Y, et al. Microglia exacerbate white matter injury via complement C3/C3aR pathway after hypoperfusion. *Theranostics.* 2020;10:74–90.
36. Gelfand JM, Cree BA, Nolan R, Arnow S, Green AJ. Microcystic inner nuclear layer abnormalities and neuromyelitis optica. *JAMA Neurol.* 2013;70:629–33.
37. Danesh H, Steel DH, Hogg J, Ashtari F, Innes W, Bacardit J, Hurlbert A, Read JCA, Kafieh R. Synthetic OCT data generation to enhance the performance of diagnostic models for neurodegenerative diseases. *Transl Vis Sci Technol.* 2022;11:10.
38. Dauby S, Dive D, Lutterli L, Andris C, Hansen I, Maquet P, Lommers E. Comparative study of AQP4-NMOSD, MOGAD and seronegative NMOSD: a single-center Belgian cohort. *Acta Neurol Belg.* 2022;122:135–44.
39. Liddelov SA, Guttenplan KA, Clarke LE, Bennett FC, Bohlen CJ, Schirmer L, Bennett ML, Munch AE, Chung WS, Peterson TC, et al. Neurotoxic reactive astrocytes are induced by activated microglia. *Nature.* 2017;541:481–7.
40. Hartmann K, Sepulveda-Falla D, Rose IVL, Madore C, Muth C, Matschke J, Butovsky O, Liddelov S, Glatzel M, Krasemann S. Complement 3(+)-astrocytes are highly abundant in prion diseases, but their abolishment led to an accelerated disease course and early dysregulation of microglia. *Acta Neuropathol Commun.* 2019;7:83.
41. Zhang M, Dai Q, Liang D, Li D, Chen S, Chen S, Han K, Huang L, Wang J. Involvement of adenosine A1 receptor in electroacupuncture-mediated inhibition of astrocyte activation during neuropathic pain. *Arq Neuropsiquiatr.* 2018;76:736–42.
42. Jiang Z, Wei S, Liu Z, Li H, Chen T. Relationship between the levels and variation of CXCL12, PDGF, CXCL14 in cerebrospinal fluid of optic neuritis and neuromyelitis optica [*Zhonghua yan ke za zhi*]. *Chinese J Ophthalmol.* 2015;51:901–6.
43. Kang H, Cao S, Chen T, Jiang Z, Liu Z, Li Z, Wei Y, Ai N, Xu Q, Lin Q. The poor recovery of neuromyelitis optica spectrum disorder is associated with a lower level of CXCL12 in the human brain. *J Neuroimmunol.* 2015;289:56–61.
44. Fonseca MI, Chu SH, Hernandez MX, Fang MJ, Modarresi L, Selvan P, MacGregor GR, Tenner AJ. Cell-specific deletion of C1qa identifies microglia as the dominant source of C1q in mouse brain. *J Neuroinflamm.* 2017;14:48.
45. Ten VS, Yao J, Ratner V, Sosunov S, Fraser DA, Botto M, Sivasankar B, Morgan BP, Silverstein S, Stark R, et al. Complement component c1q mediates mitochondria-driven oxidative stress in neonatal hypoxic-ischemic brain injury. *J Neurosci.* 2010;30:2077–87.
46. Lynch NJ, Willis CL, Nolan CC, Roscher S, Fowler MJ, Weihe E, Ray DE, Schwaeble WJ. Microglial activation and increased synthesis of complement component C1q precedes blood-brain barrier dysfunction in rats. *Mol Immunol.* 2004;40:709–16.
47. Maisam Afzali A, Stuve L, Pfaller M, Aly L, Steiger K, Knier B, Korn T. Aquaporin-4 prevents exaggerated astrocytosis and structural damage in retinal inflammation. *J Mol Med (Berl).* 2022;100:933–46.
48. Das A, Guyton MK, Smith A, Wallace Gt, McDowell ML, Matzelle DD, Ray SK, Banik NL. Calpain inhibitor attenuated optic nerve damage in acute optic neuritis in rats. *J Neurochem.* 2013;124:133–46.
49. Remlinger J, Bagnoud M, Meli I, Massy M, Hoepner R, Linington C, Chan A, Bennett JL, Enzmann V, Salmen A. Modeling MOG antibody-associated disorder and neuromyelitis optica spectrum disorder in animal models: visual system manifestations. *Neurol Neuroimmunol Neuroinflamm.* 2023;10:e200141.

Publisher's Note

Springer Nature remains neutral with regard to jurisdictional claims in published maps and institutional affiliations.